RESEARCH ARTICLE

Green route synthesis and characterization of β-Bi$_2$O$_3$/SiO$_2$ and β-Bi$_2$O$_3$/Bi$_2$O$_{2.75}$/SiO$_2$ using *Juglans regia* L. shell aqueous extract and photocatalytic properties for the degradation of RB-5

Maria Guadalupe Yañez-Cruz[1], Maricela Villanueva-Ibáñez[1*] , Fabiola Méndez-Arriaga[2], Carlos Alexander Lucho-Constantino[3], María de los Ángeles Hernández-Pérez[4], María del Rocío Ramírez-Vargas[5] and Marco Antonio Flores-González[1]

Abstract

Background: Photocatalyst oxides added with silicon improve their photocatalytic properties. In this research, nano-structured β-Bi$_2$O$_3$/SiO$_2$ and β-Bi$_2$O$_3$/Bi$_2$O$_{2.75}$/SiO$_2$ were obtained by means of a green method mediated by the using the aqueous extract of *J. regia* shell as the source of reducing biomolecules and as a natural source of plant silicon.

Method: The β-Bi$_2$O$_3$/SiO$_2$ and β-Bi$_2$O$_3$/Bi$_2$O$_{2.75}$/SiO$_2$ nanostructures were characterized by Fourier transform infra-red spectroscopy (FT-IR), Raman spectroscopy, X-ray diffraction, high-resolution transmission electron microscopy (HR-TEM), field emission scanning electron microscopy, X-ray photoelectron spectroscopy (XPS), ultraviolet–visible diffuse reflectance spectroscopy (UV–Vis DRS), and photoluminescence spectroscopy. The photocatalytic activity was measured by the degradation of Reactive Black 5 dye (RB-5).

Results: FT-IR and XPS demonstrated the presence of plant silicon in the bismuth oxide photocatalysts. HR-TEM showed that the crystal size of the as-synthesized materials is ∼ 25 nm and revealed that the β-Bi$_2$O$_3$ synthesized with ground shell extract and heat-treated at 300 °C contains the Bi$_2$O$_{2.75}$ phase. Good photocatalytic activity was found in all the studied materials; particularly, the heat-treated nanostructures showed excellent properties resulting in 92% degradation of RB-5 under UV–Vis light after 15 min of exposure, and 98% after 180 min.

Conclusions: The findings of this research suggest that the metabolites coating the Bi$_2$O$_3$, which generate a large amount of hydroxyl radicals, the plant silicon content, and the crystalline defects conferred by the synthesis medium, all contribute to the improved degradation of the azo dye, providing the nanostructures with better photocatalytic activity.

Keywords: Bi$_2$O$_3$, Biosynthesis, Photocatalytic activity, *Juglans regia* shell extract, Plant silicon

Introduction

Water pollution is a global concern because it not only affects the ecosystems' health, but also has a direct impact on water supply and the development of economic activities. Several industries use reactive azo dyes, being the textile industry the largest producer of

*Correspondence: villanueva@upp.edu.mx

[1] Laboratory of Nanotechnology, Biological Systems and Industrial Applications, Polytechnic University of Pachuca, Zempoala, Hidalgo, Mexico
Full list of author information is available at the end of the article

synthetic dyes worldwide. It is estimated that approximately 20% of the residues of these dyes reach and contaminate the environment (Chinoune et al. 2016). Several methods are employed for the removal of synthetic dyes (Piaskowski et al. 2018), but more efficient proposals are still necessary to make possible a complete and safe degradation of these contaminants from polluted water. An attractive alternative involves the use of advanced oxidation processes (AOPs), which are based on the formation of highly reactive chemical species with low selectivity, such as the hydroxyls ($\cdot$OH), superoxide (O_2^-), or hydrogen peroxide (H_2O_2). Some of the advantages of these processes include the rapid elimination of contaminants from water with minimal generation of waste, such as sludge, low generation of degradation by-products, high disinfection rates in a short period of time, low amounts of photocatalytic material needed to perform the process, and, in most cases, the potential for reuse. Among the AOPs, the photochemical and photocatalytic methods are presented as sustainable technologies for the degradation of organic compounds; however, heterogeneous photocatalysis allows the degradation and even mineralization of various organic compounds since it is a non-selective process (Naseem and Durrani 2021; Piaskowski et al. 2018).

Metal oxides are the most suitable to be used in photocatalysis because they are capable of generating charge carriers when the necessary amount of energy is applied, also they are stable, inert, resistant to photo-oxidation, and possess a wide bandgap. Furthermore, there is a growing interest in the study of these materials at the nanoscale level because they have a large surface area and, therefore, a high number of active sites (Khan et al. 2015). Lately, interest in the synthesis of various metal-based oxide systems at the nanometric scale has increased due to their increasing and varying applications in fields such as environmental remediation, targeted drug release, photoluminescent sensors for bacteria and heavy metals detection, electrochemical hydrogen storage materials, dye adsorption, and photocatalysis (Naseem and Durrani 2021).

There has been a growing interest on bismuth oxide (Bi_2O_3) nanostructures due to the characteristics they possess, such as their wide bandgap (2.58–2.85 eV), high refractive index, good electrochemical properties, and photocatalytic activity. Additionally, Bi_2O_3 has polymorphism, which means it has multiple crystalline phases, in this case five which are as follows: α-Bi_2O_3 (monoclinic), β-Bi_2O_3 (tetragonal), γ-Bi_2O_3 (body-centred cubic), δ-Bi_2O_3 (cubic), and ε-Bi_2O_3 (triclinic). Also, Bi_2O_3 has two additional non-stoichiometric phases: $Bi_2O_{2.33}$ and $Bi_2O_{2.75}$ (Zahid and Han 2021). It has been shown that the Bi_2O_3 structural phase and properties, such as its

photocatalytic activity, depend on the synthesis method, presence of crystalline defects, elemental composition, and surface characteristics. Concerning Bi_2O_3, the best photocatalytic activity occurs on its beta phase due to its bandgap being close to 2.5 eV (Cheng et al. 2010). To further improve the photocatalytic activity of these nanomaterials, the addition of silica has commanded a growing interest. This is because the presence of silica increases the thermal and chemical stability, adsorption capacity, and the number of hydroxyl radicals on the surface, thus slowing down the recombination process of the electron–hole pair, which is important in the photocatalytic process (Jayakumar et al. 2020).

Owing to the large number of applications, researchers have developed different routes to synthetize Bi_2O_3 nanostructures including precipitation, combustion, hydrothermal, flame spray pyrolysis, sol–gel and magnetron sputtering, among others (Zahid and Han 2021). However, there is a growing concern about environmental issues related to the procurement processes, which is why simple, fast, and ecological routes are being sought for the preparation of nanostructures. For this reason, the interest in the green synthesis of photocatalyst metal oxide nanoparticles such as ZnO (Basnet et al. 2018), ZnS (Samanta et al. 2017), TiO_2 (Verma et al. 2022), SnO_2 (Buniyamin et al. 2021; Matussin et al. 2020), as well as Bi_2O_3 (Karnan and Samuel 2016), through plant extracts, is constantly increasing. It is worth mentioning that the reports related to the synthesis of Bi_2O_3 nanostructures from plant extracts indicate the need for a post-synthesis heat treatment to obtain the crystalline material in the monoclinic phase (Prakash et al. 2022).

This article describes, for the first time, the biosynthesis of β-Bi_2O_3/SiO_2 and β-Bi_2O_3/SiO_2/$Bi_2O_{2.75}$ nanostructures using *J. regia* L. shell aqueous extract as the precursor. Approximately 67% of the total weight of the nut is contained in the shell, and it can be found abundantly as a by-product of the industrial processing of walnuts, these shells are primarily made up of polyphenols, gallic acid, holocellulose, cellulose and lignin. There are few studies on the silicon content of nutshells, but it is known to be distributed throughout diverse plant structures, being used by plants to reinforce and harden tissues such as the walnut shells. The characterization of the synthesized nanostructures was carried out by FT-IR, Raman spectroscopy, XRD, HR-TEM, FESEM XPS, UV–Vis DRS, and PL analysis. The aim of this study is to propose an eco-friendly and sustainable route of synthesis for nanostructured β-Bi_2O_3/SiO_2 and β-Bi_2O_3/$Bi2O_{2.75}$/SiO_2 by taking advantage of the plant silicon content of the walnut shell, and ensuring the nanostructures possess good photocatalytic properties to achieve the degradation of the azo dye Reactive Black 5 (RB-5).

Materials and methods

Chemicals

Bismuth nitrate pentahydrate ($Bi(NO_3)_3 \cdot 5H_2O$), sodium hydroxide (NaOH), hydrochloric acid (HCl), and Reactive Black 5 Dye dye were supplied by Sigma-Aldrich and used without further purification. All the aqueous solutions were freshly prepared using deionized water, and all glassware used in the experiments was washed with aqua regia and then thoroughly rinsed with deionized water.

Shell extract preparation

Whole *J. regia* shells (WL) obtained from producers in Hidalgo (Mexico) were washed with deionized water and dried at 40 °C for 72 h. The ground shells (GD) were crushed (< 420 μm) using an agate mortar. GD and WL shells were placed in deionized water (1:100) in a 40-mL vial each and heated to 90 °C maintaining this temperature for 10 min. The resulting extract was filtered using Whatman No.1 filter paper, and the filtrate was stored at 4 °C.

Biosynthesis of Bi_2O_3 nanostructures

Half a millilitre of each of the two extracts was added to 5 mL of $Bi(NO_3)_3 \cdot 5H_2O$ (6 mM), and the pH was adjusted to 7 by adding NaOH (2 M) under stirring at 25 °C for 4 h. The resulting solution changed colour to light brown due to the formation of Bi_2O_3 nanostructures, called BGD and BWL when obtained with GD and WL extracts, respectively. Samples were centrifuged at 8000 rpm for 10 min, rinsed three times with deionized water, and dried at 40 °C. For photocatalytic tests, BGD and BWL were heat-treated at 300 °C for 1 h (named BGD3 and BWL3 after the process) to promote higher crystallinity. The biosynthesized nanostructures were stored in a dry and dark place for further characterization.

Characterization

Qualitative phytochemical screening using standard procedures was carried out to identify the type of secondary metabolites present in the plant extracts. Functional groups in both extracts of *J. regia* and in the nanostructures were identified by FT-IR spectroscopy (PerkinElmer 2000) in the scanning range of 4000–400 cm^{-1} using an attenuated total reflectance (ATR) cell for spectral recording. The crystalline structure of the nanostructures was studied by XRD (Bruker-D8) using Cu Kα = 1.5496 Å at 2θ range from 20 to 80°. In order to investigate the presence of crystalline defects, Raman spectra were collected in the range of 30–800 cm^{-1} using an XploRA Plus ONE™

spectrometer with a 532 nm laser source and PL spectra were recorded with a Fluorolog-3 ($\lambda_{ex} = 290$ nm). The bandgap was determined by UV–Vis DRS (PerkinElmer Lambda 300). The morphology was examined by FESEM (JEOL-JSM-6701F) and HR-TEM (JEM-2100) with an accelerating voltage of 200 kV; the image analysis by fast Fourier transform (FFT) was carried out using Digital Micrograph 3.7.0 software (Gatan Software, Inc., Pleasanton, CA, USA). The elemental and chemical composition was analysed by X-ray photoelectron spectroscopy (XPS) in a Thermo Scientific spectrometer equipped with a monochromatic Al Kα X-ray source (1486.6 eV).

RB-5 degradation

The photocatalytic activity of the samples (1 g/L) was examined by degrading RB-5 at a concentration of 15 mg/L, the pH of the medium was set to 9 according to the point of zero charge (PZC) of the Bi_2O_3 nanostructures, and the system was kept at a stirring rate of 300 rpm at room temperature. For the adsorption process, the reaction system was kept in the dark for 30 min, and about 5 mL of aliquot samples was centrifuged at 8000 rpm for 10 min to remove the sorbent. The concentration of RB-5 in the solution was determined spectrophotometrically by measuring the absorbance at 598 nm at room temperature in a quartz cuvette using Cole-Parmer 2800 UV–Vis spectrophotometer. Then, the solution was exposed to the UV–Vis light (300 W HP Hg Lamp), and at 0, 15, 30, 45, 60, 90, 120, 150, and 180 min time intervals, 5 mL aliquots were taken and centrifuged under the same conditions to remove solid particles. The degradation efficiency was calculated using Eq. (1):

$$\eta = \frac{C_0 - C}{C_0} \times 100 \tag{1}$$

where C_0 stands for the initial concentration and C for the concentration at any given time. A control experiment was carried out with the dye and without any photocatalyst, after the set time.

Results and discussion

Characterization of *J. regia* shell extract and Bi_2O_3 nanostructures

The GD and WL extract were qualitatively analysed to determine their phytochemical constituents. This study revealed the presence of secondary metabolites in both extracts, such as saponins, carbohydrates, and reducing sugars; tannins were only identified in GD. These results are consistent with those obtained by Sze-Tao et al. (2001), who studied the content of tannins in walnut shells and concluded that the bioavailability of phenolic compounds is favoured by decreasing the particle size of
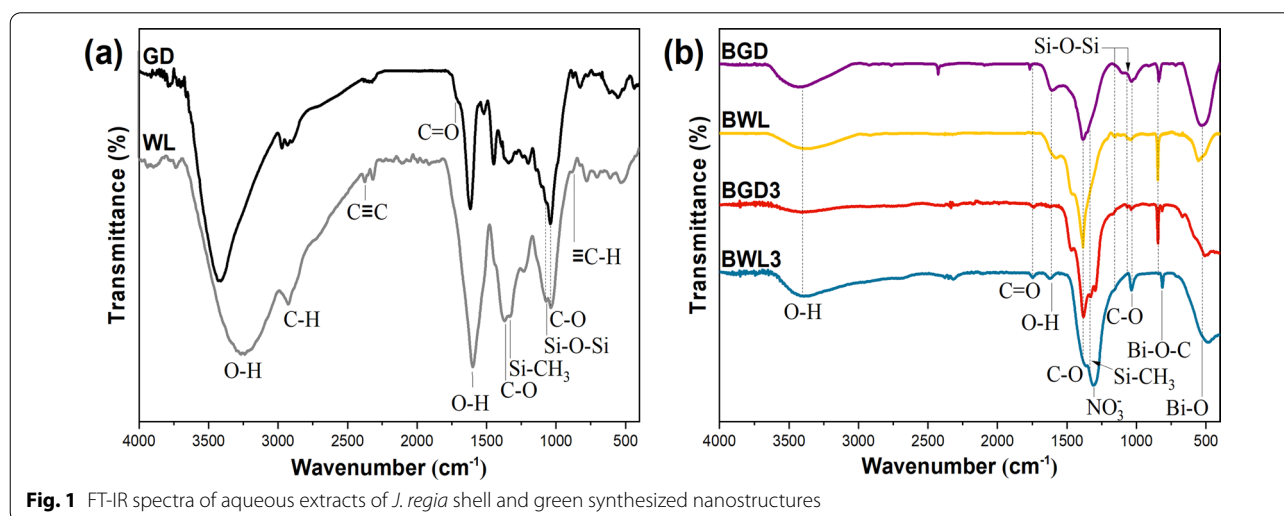
the biomass. Tannins are one of the most important phenolic compounds in the reduction of salts and stabilization of nanoparticles.

Identification of the functional groups and the presence of silicon in the extract was carried out by FT-IR, this technique was also used to verify the possible interaction between the extract and the nanostructures. The FT-IR spectra of aqueous GD and WL extracts are shown in Fig. 1a. The bands located at 3239 cm^{-1} and 1600 cm^{-1} can be attributed to O–H stretching vibrations and indicate the presence of a large number of hydroxyl groups. The band at 2926 cm^{-1} corresponds to the aliphatic stretching vibrations of $-CH_2$ CH_3, and the bands around 2375 cm^{-1} denote the C≡C vibration. The peak at 1711 cm^{-1} overlaps with the O–H groups and can be attributed to the C=O stretching of the carbonyl group. Bands at 1369 cm^{-1} are indicative of C–O stretching related to alcohol, carboxylic acid, ester, and ether. The characteristic peak at 1041 cm^{-1} corresponds to the C–O stretching associated with the carbohydrate content. The bands between 534 and 884 cm^{-1} are due to the stretching vibration of the ≡C–H of phenolic-based compounds, such as the band at 775 cm^{-1}, related to juglone, the walnut shell pigment (Li et al. 2020; Uddin and Nasar 2020). Among the differences observed between the two spectra, it must be noted that some bands were not present in WL, and the relative intensity of others was lower, especially those associated with phenolic compounds, which can influence the formation of Bi$_2$O$_3$. Likewise, FT-IR analysis revealed that the extracts contained silicon compounds. The peak at 1071 cm^{-1} that overlaps with the C-O bond signal located at 1041 cm^{-1}, as well as the bands located between 800 and 400 cm^{-1}, can be attributed to the siloxane bond (Si–O–Si) (Hosseini Mohtasham and Gholizadeh 2020). Similarly, the peaks located in 1331, 1341, 1233, and 1090 cm^{-1} have been reported to belong to the Si-CH$_3$ bond (Akhayere et al. 2019; Członka et al. 2020).

The FT-IR spectra of Bi$_2$O$_3$ nanostructures (BGD, BWL, BGD3, and BWL3) are shown in Fig. 1b, where the peak located at 1306 cm^{-1} corresponds to NO$_3^-$ (Yan et al. 2014) and the peaks at 845 cm^{-1} and 552 cm^{-1} are due to the presence of Bi–O–C and Bi–O, respectively (Indurkar et al. 2018). Just as in the spectra of the extracts, the bands at 3401, 1613, and 1746 cm^{-1} indicate the presence of hydroxyl and carbonyl groups; these results suggest that residues of organic compounds of the extract remain on the surface of the Bi$_2$O$_3$ nanostructures after fulfilling their roles as reducers of the precursor salt and stabilizers of the obtained nanostructures. Only BGD3 showed both peaks related to the presence of silicon compounds at 1331 and 1064 cm^{-1}, attributed to Si–O–Si and Si–CH$_3$ (Członka et al. 2020).

To determine the crystal structure and to estimate the crystal size, an XRD technique was used; Fig. 2a shows the XRD patterns of the as-synthesized Bi$_2$O$_3$ nanostructures. The diffractograms obtained from BGD and BWL resemble those of amorphous materials or nanoparticles smaller than 3 nm. In both extracts, the broad diffraction peak at 28° is attributed to residues of the extract of *J. regia* (Izadiyan et al. 2018). On the other hand, in the BGD3 and BWL3 samples, all the 2θ peaks observed at 27.9°, 31.7°, 32.6, 46.2°, 46.9°, 54.2°, 55.4°, 55.6°, 57.7°, 74.4°, 75.5°, and 75.9° are consistent with the (201), (002), (220), (222), (400), (203), (421), (213), (402), (610), (601), and (224) lattice planes and can be indexed as β-Bi$_2$O$_3$ (JCPDS card No. 00-027-0050). From the XRD data, the crystal size of the samples was estimated using Scherrer's equation (Patterson 1939); the average size for the BGD3 and BWL3 samples was
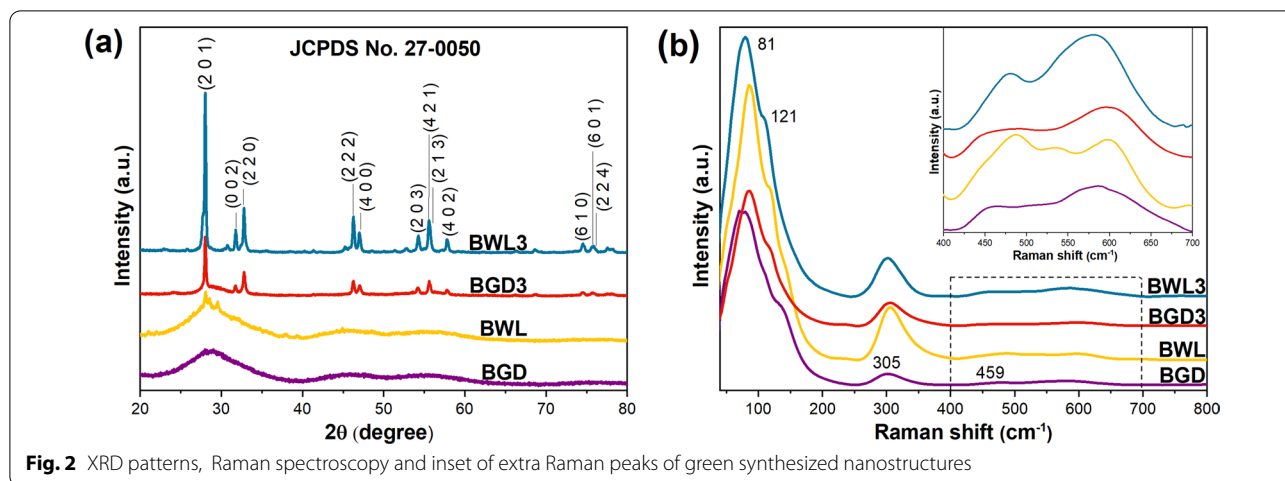

Fig. 1 FT-IR spectra of aqueous extracts of *J. regia* shell and green synthesized nanostructures

Fig. 2 XRD patterns, Raman spectroscopy and inset of extra Raman peaks of green synthesized nanostructures

about 28 and 31 nm, respectively. Although X-ray diffraction is one of the most widely used techniques to characterize the crystalline structure of materials, additional analyses are needed to obtain complementary information on the crystallinity of these biosynthesized materials (Mourdikoudis et al. 2018). The Raman spectra shown in Fig. 2b displayed identical peaks along all samples; the peak at 81 cm^{-1} is related to the Eg phonon mode of the rhombohedral Bi, and peaks at 121, 305, and 459 cm^{-1} correspond to the Bi-O stretching modes of Bi_2O_3 (Díaz-Guerra et al. 2017). The displacement of and extra Raman peaks at 520–590 cm^{-1} (inset of Fig. 2b) are associated with oxygen vacancies (Gavarri et al. 2009); these vacancies improve photocatalytic activity, since they work as a trap for the photogenerated electrons, delaying or preventing the
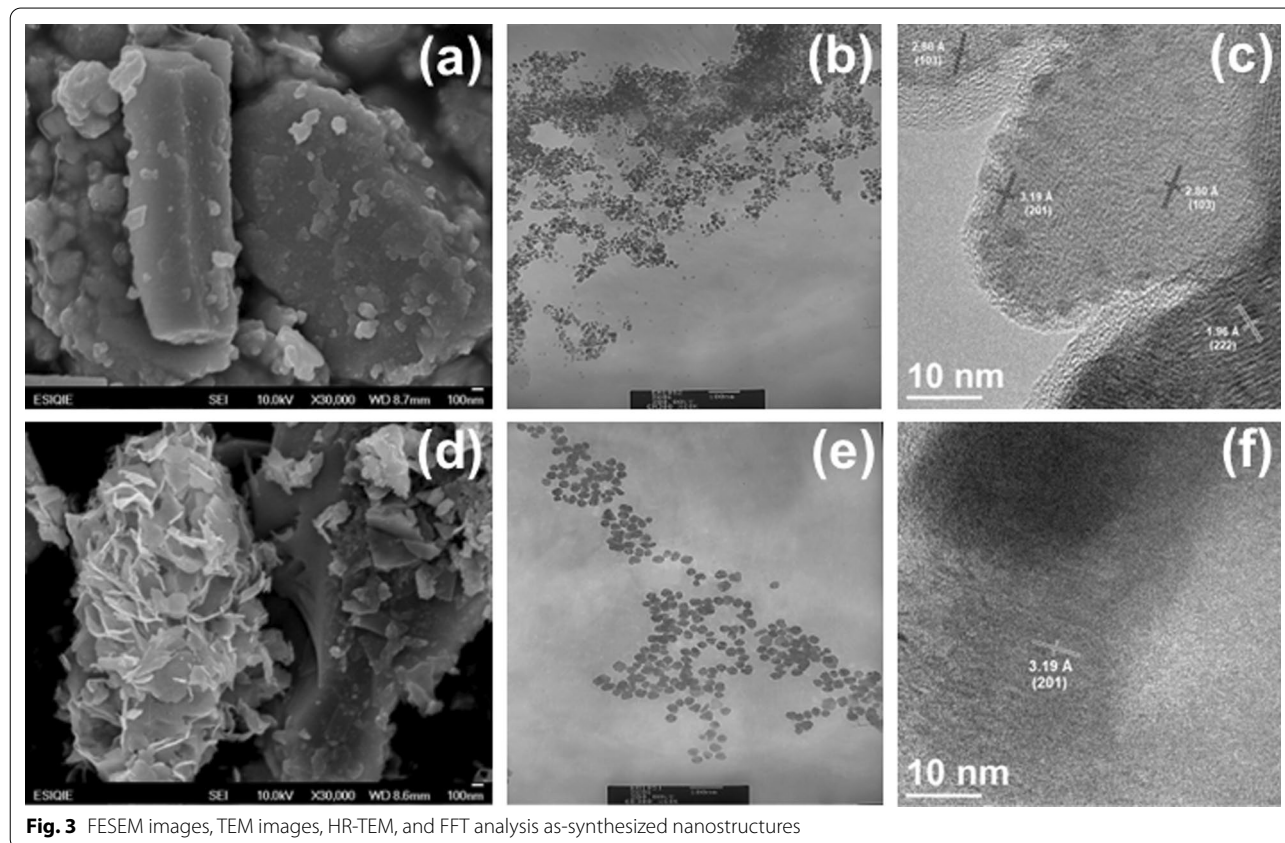

Fig. 3 FESEM images, TEM images, HR-TEM, and FFT analysis as-synthesized nanostructures
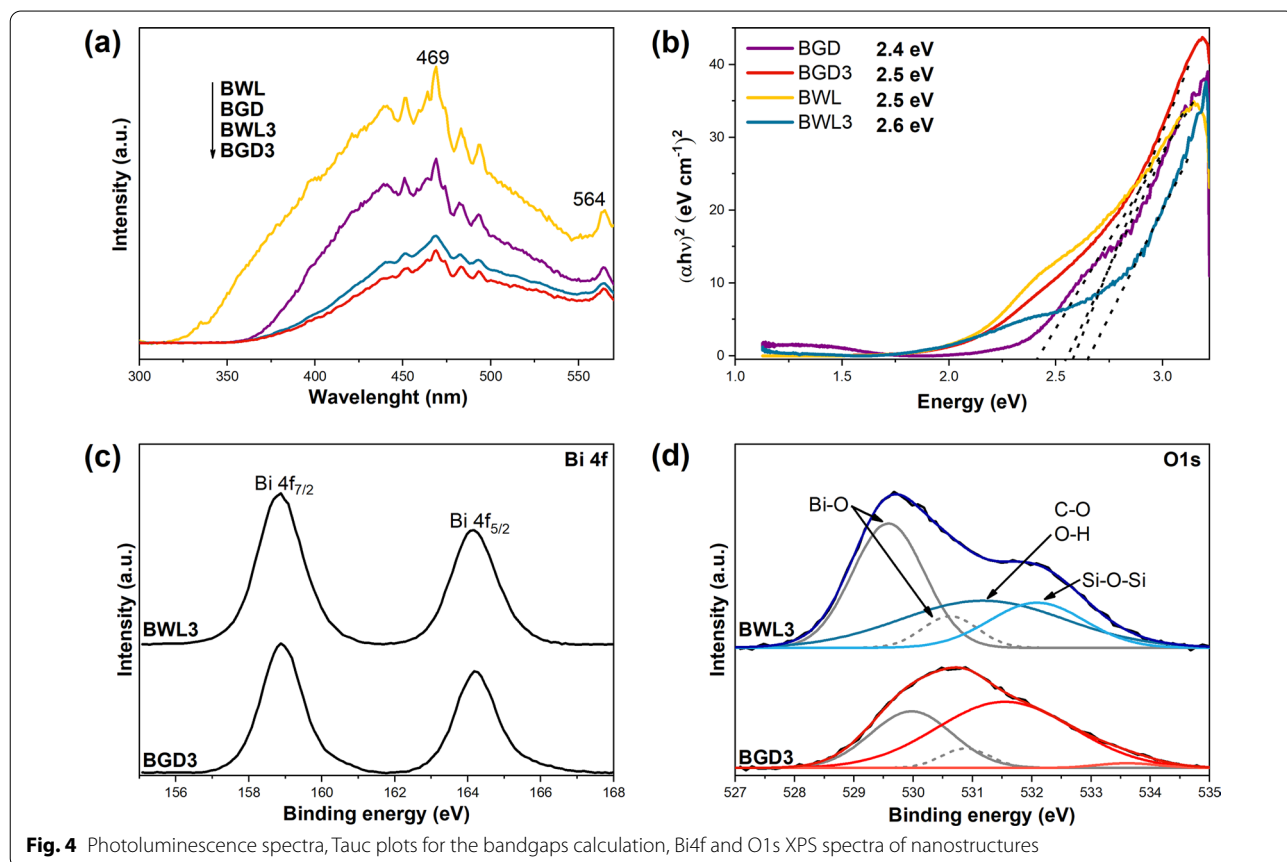
recombination process, and allowing redox reactions to take place (Gaidau et al. 2017).

The morphology of the biosynthesized materials was analysed using FESEM images, as shown in Fig. 3a, d. The BGD3 sample shows a heterogeneous particle morphology consisting of nanorods with irregularly shaped structures on its surface, while for BWL3, it displays nanosheets with a thickness of ~25 nm. By using FESEM, it is possible to observe the coating of the biosynthesized nanostructures; this coating comes from the extracts of the WL and GD shell of *J. regia*. The presence of this layer confirms the role played by the extract in the synthesis and stabilization of the nanostructures (Oves et al. 2018).

Figure 3b, e shows TEM images where a semi-spherical morphology is observed, with a crystal distribution of ~25 nm which is in accordance with the results obtained by using Scherrer's equation from the XRD pattern. Figure 3c, f shows the HR-TEM micrographs of the as-synthesized Bi_2O_3 nanostructures. The interplanar distance d_{hkl}, measured for BWL3 by means of FFT, was $=3.19$ Å. The result is a good match with the (201) plane of β-Bi_2O_3 according to the JCPDS 00-027-0050 card, confirming their crystalline nature. Only sample BGD3 displays the coexistence of the β-Bi_2O_3

and $Bi_2O_{2.75}$ phases with $d_{hkl} = 3.19$ Å and 1.96 Å from the (201) and (222) planes from β-Bi_2O_3 JCPDS 00-027-0050 and $d_{hkl} = 2.80$ Å from the $Bi_2O_{2.75}$ phase (JCPDS 00-027-0049); just as with β-Bi_2O_3, the $Bi_2O_{2.75}$ phase has shown excellent photocatalytic degradation of azo dyes (Wang et al. 2019; Zhou et al. 2020). The results indicate that the smallest spherical particles of non-crystalline material immersed in BGD3 (Fig. 3c) could correspond to the silicon compounds (Chen et al. 2017) from the aqueous extract of *J. regia* used in the synthesis.

The separation efficiency of photogenerated electron–hole pairs of biosynthesized materials was analysed using PL spectroscopy (Fig. 4a) where identical spectra are shown, but with different intensities of exciton photoluminescence. The emission at 469 nm is attributed to the intra-ionic transitions of Bi^{3+} or to surface and interface states due to crystalline defects, such as oxygen vacancies (Hariharan and Karthikeyan 2018), and the peak at 564 nm is related to the electrovalence of Bi ions (Labib 2017). It is well known that high PL emission intensities represent a greater recombination of charge carriers. The decrease in intensity at 469 and 564 nm for BGD3 means that direct electron

Fig. 4 Photoluminescence spectra, Tauc plots for the bandgaps calculation, Bi4f and O1s XPS spectra of nanostructures

and hole recombination is avoided (Cheng et al. 2010) which is beneficial to the improvement in the photocatalytic activity.

UV–Vis DRS was performed to study the optical properties of the biosynthesized nanomaterials. The direct bandgaps (Fig. 4b) were calculated using the Tauc Eq. (2)

$$\alpha h\nu = A(h\nu - E_g)^2 \qquad (2)$$

where α is the absorption coefficient, A is a constant, h is Planck's constant, ν is the light frequency of photons, and Eg is the bandgap (Yan et al. 2014). The plots of $(\alpha h\nu)^2$ versus (hv) show large Urbach tails for each material. The bandgap values were 2.4, 2.5, 2.5, and 2.6 eV, for BGD, BWL, BGD3, and BWL3, respectively. The slight variation in these values can be explained by the difference in the degree of absorption of visible light due to these Urbach tails (Yaghoubi et al. 2015) caused by different interactions closely related to the formation of new phases, in this case the non-stoichiometric phase (Leontie et al. 2002; Wang et al. 2019; Zhou et al. 2020), which tends to shift towards the red; oxygen vacancies, derived from the synthesis method (Stan et al. 2015), crystallinity (Huang et al. 2011), morphology and particle size (Labib 2017), as well as the content of silicon and its interaction with Bi_2O_3 (Wu et al. 2006) also contribute to the variations. All biosynthesized photocatalysts have a low band gap value, which allows them to be irradiated, thus permitting them to take advantage of the spectrum of sunlight which is an improvement on the other Bi_2O_3 phases.

The chemical surface compositions of BGD3 and BWL3 were qualitatively analysed by XPS. The high-resolution spectra of Bi4f in Fig. 4c show bands located at 158.86 and 164.13 eV, and at 158.88 and 164.20 eV; these are attributed to Bi 4f7/2 and Bi 4f5/2, respectively, suggesting that the Bi was in its Bi^{3+} state. The energy difference of 5.27 and 5.32 eV is consistent with the spin–orbit splitting value (5.3 eV) for Bi_2O_3 (Zhou et al. 2020). Figure 4d displays the O1s asymmetrical signal, which can be separated into four peaks; those located at lower binding energies (529.58, 529.97 and 530.62, 530.88 eV) can be attributed to lattice oxygen Bi-O while the ones found at higher energies (531.17, 531.54 eV) correspond to adsorbed oxygen, in this case from the mixed contributions of O–H and C-O groups of the metabolites surrounding the nanostructures. The peaks at 532.08 and 533.61 eV are associated with Si–O-Si linkages (D. Yang et al. 2011). Although *J. regia* shell silicon has not been formally reported, these results confirm the existence of plant silicon in the Bi_2O_3 synthesized from the aqueous extracts of the *J. regia* shell.

Silicon is not essential for plants, but it has an important role in their morphological and physiological properties. It is first absorbed by the roots and then it is transported to the foliar tissues in the form of silicic acid, where it accumulates without being toxic. Instead of harming the plant, the silicon self-regulates, polymerizing into phytolites, which provide greater structure rigidity and allow better use of light (Deshmukh et al. 2017). Plant silicon has been extensively studied and it has been found that there are species that store it in large quantities; however, little attention has been paid to the existence of this element in the extracts used for the synthesis of nanomaterials. If plant silicon is present in the biosynthesis processes, it could modify the properties of the resulting photocatalysts since it is known that the chemical addition of silicon to TiO_2 and Bi_2O_3 can improve their activity, conferring thermal stability and increasing the formation of reactive oxygen species (Gaidau et al. 2017; Jayakumar et al. 2020; J. Yang et al. 2014).

Photocatalytic degradation of RB-5

The release of RB-5 in textile effluents represents a significant threat to health due to the resulting pollution in rivers; even at low concentrations, it is toxic and is capable of staining large amounts of water; furthermore, it blocks sunlight from reaching river beds suppressing photosynthetic processes and reducing dissolved oxygen (Munagapati et al. 2020). The UV–Vis spectra of RB-5
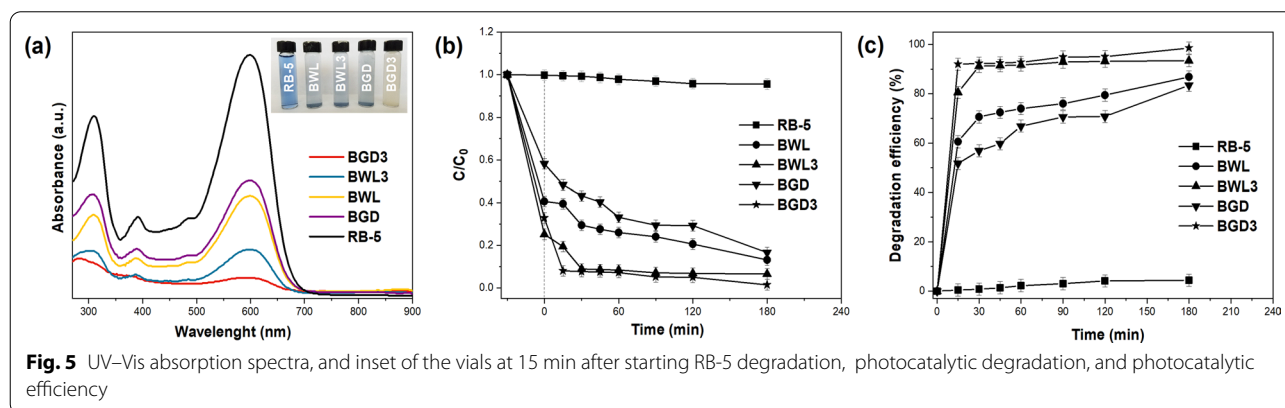
Fig. 5 UV–Vis absorption spectra, and inset of the vials at 15 min after starting RB-5 degradation, photocatalytic degradation, and photocatalytic efficiency

exhibit two main absorption bands at 312 nm in the UV region and at 598 nm in the visible region, corresponding to naphthalene and the chromophore group (-N=N), these are used to measure the decolourization of the dye solution. Figure 5a and its inset show the UV–Vis absorption spectra as well as the vials 15 min after starting the RB-5 degradation process with the different photocatalysts under simulated UV–Vis light. No degradation was observed in the control experiment, indicating that RB-5 is stable to self-photodegradation. When the synthesized catalysts were tested, the main absorption bands of the dye decreased considerably, disappearing almost completely when using the BGD3 catalyst. Figure 5b shows the photodegradation of RB-5 as a function of irradiation time over 180 min. All the photocatalysts had the ability to degrade RB-5; however, the process was favoured by the materials that were heat-treated at 300 °C. The BGD3 sample showed the highest degradation with 92% after 15 min and 98% 180 min after starting the process (Fig. 5c). No new absorption peaks were observed after the tests, indicating that no new products or intermediates were formed. The theoretical degradation pathway of RB-5 from previous reports is found in the supplementary material to this paper (Additional file 1: Figure S1). The difference in degradation efficiency between the employed catalysts can mainly be attributed to their optical properties and the pH of the aqueous dye solution, which plays an important role in the photocatalytic activity of the biosynthesized catalysts. This leads to the PZC which is the pH value at which the total net charge of the catalyst is neutral and it determines the catalyst's interaction with the dye. The PZC values of the thermal treated and untreated catalysts were 11.5 and 8.2, respectively, at lower pH values they will have a positively charged surface and, at higher values, a negative charge. Considering that RB-5 has a negative charge due to the presence of sulphonate groups (SO^{3-}) (Netpradit et al. 2004) and that the experiments in this study were carried out at pH 9, the degradation of the dye was favoured by the heat-treated catalysts. This is because at this pH value the heat-treated catalysts have a positive surface charge and RB-5 is more easily adsorbed with the aid of the electrostatic attraction (Aguiar et al. 2014). Additionally, it can be observed that the catalysts obtained with ground shells (BGD and BGD3) had a higher silicon content and a better photocatalytic activity when compared to those obtained with whole shells (BWL and BWL3).

In the last decade, several studies have been conducted on obtaining biogenic silica from agro-industrial residues and how its addition to catalysts improve their photocatalytic properties when compared to silica-free photocatalysts (Mattos et al. 2017; Yang et al. 2011; Fatimah et al. 2019); however, a calcination process followed by

an acid extraction is necessary to extract the plant silica. It should be noted that in this research no additional method was used for the extraction of silicon during the preparation of the plant aqueous extract. These results set a precedent for the detailed study of the composition of extracts containing silicon used in the biosynthesis of photocatalysts as well as the silicon relationship with the catalyst properties. Also, it gives insight into the design of an improved photocatalyst with low environmental impact.

Conclusions

Nanostructured β-Bi_2O_3/SiO_2 and β-Bi_2O_3/$Bi_2O_{2.75}$/SiO_2 were successfully synthesized using a green synthetic route with *J. regia* shell extract. Secondary metabolites such as saponins, carbohydrates, reducing sugars, and tannins act as reducing and capping agents in Bi_2O_3 formation. The use of this extract as a means of synthesis of Bi_2O_3 favours crystalline defects that delay the recombination of the electron–hole pair. Applying a heat treatment of 300 °C to the nanostructures obtained from the ground shell extract was sufficient to obtain β-Bi_2O_3/$Bi_2O_{2.75}$, which, together with the plant silica, improved photocatalysis efficiency achieving a 98% degradation of RB-5 throughout the 180-min process. These results set a precedent for the study of metabolites availability and silicon content in plant extracts obtained from agro-industrial waste, as well as their use in the synthesis of nanomaterials and their positive effect on said nanomaterials photocatalytic properties when used for the removal of dyes in aqueous solutions.

Supplementary Information

The online version contains supplementary material available at https://doi.org/10.1186/s40543-022-00355-0.

Additional file 1. Proposed photocatalytic degradation mechanism for the azo dye, reactive black 5 with TiO_2 and ZnO-based catalysts.

Author contributions
MVI, as the main researcher, contributed to the design of the study and acted as supervisor of the methodology conceptualization, data analysis, and manuscript preparation/revision. MGYC, as the first author, carried out the

Yañez-Cruz *et al. Journal of Analytical Science and Technology*   (2022) 13:52

Page 9 of 10

Declarations

Ethics approval and consent to participate
Not applicable.

Consent for publication
Not applicable.

Competing interests
The authors declare that they have no competing interests.

Author details
[1]Laboratory of Nanotechnology, Biological Systems and Industrial Applications, Polytechnic University of Pachuca, Zempoala, Hidalgo, Mexico. [2]Institute for Applied Sciences and Technology-National Council for Science and Technology, National Autonomous University of Mexico, Coyoacán, Mexico City, Mexico. [3]Chemistry Academic Area, Autonomous University of the State of Hidalgo, Pachuca, Hidalgo, Mexico. [4]Department of Metallurgy and Materials Engineering, ESIQIE, National Polytechnic Institute, Mexico City, Mexico. [5]Department of Biotechnology Engineering, Polytechnic University of Pachuca, Zempoala, Hidalgo, Mexico.

References

Aguiar JE, Bezerra BTC, Siqueira ACA, Barrera D, Sapag K, Azevedo DCS, et al. Improvement in the adsorption of anionic and cationic dyes from aqueous solutions: a comparative study using aluminium pillared clays and activated carbon. Sep Sci Technol. 2014;49(5):741–51.

Akhayere E, Kavaz D, Vaseashta A. Synthesizing nano silica nanoparticles from barley grain waste: effect of temperature on mechanical properties. Polish J Environ Stud. 2019;28(4):2513–21.

Basnet P, Inakhunbi Chanu T, Samanta D, Chatterjee S. A review on bio-synthesized zinc oxide nanoparticles using plant extracts as reductants and stabilizing agents. J Photochem Photobiol B Biol. 2018;183:201–21.

Buniyamin I, Md Akhir R, Asnida Asli N, Khusaimi Z, Rusop MM. Biosynthesis of SnO_2 nanoparticles by aqueous leaves extract of *Aquilaria malaccensis* (agarwood). IOP Conf Ser Mater Sci Eng. 2021;1092(1): 012070.

Chen K, Fan W, Huang C, Qiu X. Enhanced stability and catalytic activity of bismuth nanoparticles by modified with porous silica. J Phys Chem Solids. 2017;110(May):9–14.

Cheng H, Huang B, Lu J, Wang Z, Xu B, Qin X, et al. Synergistic effect of crystal and electronic structures on the visible-light-driven photocatalytic performances of Bi_2O_3 polymorphs. Phys Chem Chem Phys. 2010;12(47):15468–75.

Chinoune K, Bentaleb K, Bouberka Z, Nadim A, Maschke U. Adsorption of reactive dyes from aqueous solution by dirty bentonite. Appl Clay Sci. 2016;123:64–75.

Członka S, Strąkowska A, Kairytė A. Effect of walnut shells and silanized walnut shells on the mechanical and thermal properties of rigid polyurethane foams. Polym Test. 2020;87: 106534.

Deshmukh RK, Ma JF, Bélanger RR. Editorial: role of silicon in plants. Front Plant Sci. 2017;8:1–3.

Díaz-Guerra C, Almodóvar P, Camacho-López M, Camacho-López S, Piqueras J. Formation of β-Bi_2O_3 and δ-Bi_2O_3 during laser irradiation of Bi films studied in-situ by spatially resolved Raman spectroscopy. J Alloys Compd. 2017;723:520–6.

Fatimah I, Prakoso NI, Sahroni I, Musawwa MM, Sim YL, Kooli F, et al. Physicochemical characteristics and photocatalytic performance of TiO_2/SiO_2 composite catalyst synthesized using biogenic silica from bamboo leaves. Heliyon. 2019;5(11): e02766.

Gaidau C, Petica A, Ignat M, Popescu LM, Piticescu RM, Tudor IA, et al. Preparation of silica doped titania nanoparticles with thermal stability and photocatalytic properties and their application for leather surface functionalization. Arab J Chem. 2017;10(7):985–1000.

Gavarri JR, Bourja L, Bakiz B, Benlhachemi A, Ezahri M, Valmalette JC, et al. Structural and raman vibrational studies of CeO_2–Bi_2O_3 oxide system. Adv Mater Sci Eng. 2009;2009:1–4.

Hariharan S, Karthikeyan B. Environment dependent enhanced photoluminescence and Boolean logic gates like behavior of Bi_2O_3 and Ag:Bi_2O_3 nanostructures. Spectrochim Acta - Part A Mol Biomol Spectrosc. 2018;193:344–8.

Hosseini Mohtasham N, Gholizadeh M. Nano silica extracted from horsetail plant as a natural silica support for the synthesis of H3PW12O40 immobilized on aminated magnetic nanoparticles (Fe_3O_4@SiO_2-EP-NH-HPA): a novel and efficient heterogeneous nanocatalyst for the green one-pot synthesis o. Res Chem Intermed. 2020;46(6):3037–66.

Huang Q, Zhang S, Cai C, Zhou B. β and α-Bi_2O_3 nanoparticles synthesized via microwave-assisted method and their photocatalytic activity towards the degradation of rhodamine B. Mater Lett. 2011;65(6):988–90.

Indurkar AR, Sangoi VD, Patil PB, Nimbalkar MS. Rapid synthesis of Bi_2O_3 nanoneedles via 'green route' and evaluation of its anti-fungal activity. IET Nanobiotechnol. 2018;12(4):496–9.

Izadiyan Z, Shameli K, Hara H, Mohd Taib SH. Cytotoxicity assay of biosynthesis gold nanoparticles mediated by walnut (*Juglans regia*) green husk extract. J Mol Struct. 2018;1151:97–105.

Jayakumar S, Saravanan T, Philip J. Polymer nanocomposites containing β-Bi_2O_3 and silica nanoparticles: Thermal stability, surface topography and X-ray attenuation properties. J Appl Polym Sci. 2020;137(36):1–11.

Karnan T, Samuel S. A novel bio-mimetic approach for the fabrication of Bi_2O_3 nanoflakes from rambutan (*Nephelium lappaceum* L.) peel extract and their photocatalytic activity. Ceram Int. 2016;42(4):4779–87.

Khan MM, Adil SF, Al-Mayouf A. Metal oxides as photocatalysts. J Saudi Chem Soc. 2015;19(5):462–4.

Labib S. Preparation, characterization and photocatalytic properties of doped and undoped Bi_2O_3. J Saudi Chem Soc. 2017;21(6):664–72.

Leontie L, Caraman M, Alexe M, Harnagea C. Structural and optical characteristics of bismuth oxide thin films. Surf Sci. 2002;507–510:480–5.

Li X, Qiu J, Hu Y, Ren X, He L, Zhao N, et al. Characterization and comparison of walnut shells-based activated carbons and their adsorptive properties. Adsorpt Sci Technol. 2020;38(9–10):450–63.

Mattos BD, Rojas OJ, Magalhães WLE. Biogenic silica nanoparticles loaded with neem bark extract as green, slow-release biocide. J Clean Prod. 2017;142:4206–13.

Matussin S, Harunsani MH, Tan AL, Khan MM. Plant-extract-mediated SnO_2 nanoparticles: synthesis and applications. ACS Sustain Chem Eng. 2020;8(8):3040–54.

Mourdikoudis S, Pallares RM, Thanh NTK. Characterization techniques for nanoparticles: comparison and complementarity upon studying nanoparticle properties. Nanoscale. 2018;10(27):12871–934.

Munagapati VS, Wen JC, Pan CL, Gutha Y, Wen JH, Reddy GM. Adsorptive removal of anionic dye (Reactive Black 5) from aqueous solution using chemically modified banana peel powder: kinetic, isotherm, thermodynamic, and reusability studies. Int J Phytoremediation. 2020;22(3):267–78.

Naseem T, Durrani T. The role of some important metal oxide nanoparticles for wastewater and antibacterial applications: a review. Environ Chem Ecotoxicol. 2021;3:59–75.

Netpradit S, Thiravetyan P, Towprayoon S. Adsorption of three azo reactive dyes by metal hydroxide sludge: Effect of temperature, pH, and electrolytes. J Colloid Interface Sci. 2004;270(2):255–61.

Oves M, Aslam M, Rauf MA, Qayyum S, Qari HA, Khan MS, et al. Antimicrobial and anticancer activities of silver nanoparticles synthesized from the root hair extract of Phoenix dactylifera. Mater Sci Eng C Mater Biol Appl. 2018;89:429–43.

Patterson AL. The scherrer formula for X-ray particle size determination. Phys Rev. 1939;56(10):978–82.

Piaskowski K, Świderska-Dąbrowska R, Zarzycki PK. Dye removal from water and wastewater using various physical, chemical, and biological processes. J AOAC Int. 2018;101(5):1371–84.

Prakash M, Kavitha HP, Abinaya S, Vennila JP, Lohita D. Green synthesis of bismuth based nanoparticles and its applications - A review. Sustain Chem Pharm. 2022;25: 100547.

Samanta D, Chanu TI, Chatterjee S. Citrus limetta juice as capping agent in hydrothermal synthesis of ZnS nanosphere for photocatalytic activity. Mater Res Bull. 2017;88:85–90.

Stan M, Popa A, Toloman D, Dehelean A, Lung I, Katona G. Enhanced photocatalytic degradation properties of zinc oxide nanoparticles synthesized by using plant extracts. Mater Sci Semicond Process. 2015;39:23–9.

Sze-Tao KWC, Schrimpf JE, Teuber SS, Roux KH, Sathe SK. Effects of processing and storage on walnut (*Juglans regia* L) tannins. J Sci Food Agric. 2001;81(13):1215–22.

Uddin MK, Nasar A. Walnut shell powder as a low-cost adsorbent for methylene blue dye: isotherm, kinetics, thermodynamic, desorption and response surface methodology examinations. Sci Rep. 2020;10(1):1–13.

Verma V, Al-Dossari M, Singh J, Rawat M, Kordy MGM, Shaban M. A review on green synthesis of TiO_2 NPs: synthesis and applications in photocatalysis and antimicrobial. Polymers (basel). 2022;14(7):1444.

Wang M, Tan G, Zhang D, Li B, Lv L, Wang Y, et al. Defect-mediated Z-scheme BiO_{2-x}/$Bi_2O_{2.75}$ photocatalyst for full spectrum solar-driven organic dyes degradation. Appl Catal B Environ. 2019;254:98–112.

Wu Q, Li D, Chen Z, Fu X. New synthesis of a porous Si/TiO_2 photocatalyst: testing its efficiency and stability under visible light irradiation. Photochem Photobiol Sci. 2006;5(7):653–5.

Yaghoubi H, Li Z, Chen Y, Ngo HT, Bhethanabotla VR, Joseph B, Ma S, Schlaf R, Takshi A. Toward a visible light-driven photocatalyst: the effect of midgap-states-induced energy gap of undoped TiO_2 nanoparticles. Am Chem Soc Catal. 2015;5:327–35.

Yan Y, Zhou Z, Cheng Y, Qiu L, Gao C, Zhou J. Template-free fabrication of α and β-Bi_2O_3 hollow spheres and their visible light photocatalytic activity for water purification. J Alloys Compd. 2014;605:102–8.

Yang D, Fan T, Zhou H, Ding J, Zhang D. Biogenic hierarchical TiO_2/SiO_2 derived from rice husk and enhanced photocatalytic properties for dye degradation. PLoS ONE. 2011;6(9): e24788.

Yang J, Wang X, Dai J, Li J. Efficient visible-light-driven photocatalytic degradation with Bi_2O_3 coupling silica doped TiO_2. Ind Eng Chem Res. 2014;53:12575–86.

Zahid AH, Han Q. A review on the preparation, microstructure, and photocatalytic performance of Bi_2O_3 in polymorphs. Nanoscale. 2021;13(42):17687–724.

Zhou G, Huang Y, Wei D, Fan Z, Seo HJ. Solvothermal synthesis, morphology, and optical properties of Bi_2O_3 and Bi/$Bi_2O_{2.75}$ powders. J Nanoparticle Res. 2020;22(15):1–12.

Publisher's Note